The EBLM project – VII. Spin–orbit alignment for the circumbinary planet host EBLM J0608-59 A/TOI-1338 A

Vedad Kunovac Hodžić [1,2]*†, Amaury H. M. J. Triaud [1]*, David V. Martin [3]‡, Daniel C. Fabrycky,[2] Heather M. Cegla [4,5], Andrew Collier Cameron [6], Samuel Gill,[4] Coel Hellier,[7] Veselin B. Kostov,[8,9] Pierre F. L. Maxted,[7] Jerome A. Orosz,[10] Francesco Pepe,[5] Don Pollacco,[4] Didier Queloz,[5,11] Damien Ségransan,[5] Stéphane Udry[5] and William F. Welsh[10]

[1]*School of Physics and Astronomy, University of Birmingham, Edgbaston, Birmingham B15 2TT, UK*
[2]*Department of Astronomy and Astrophysics, University of Chicago, 5640 S. Ellis Avenue, Chicago, IL 60637, USA*
[3]*Department of Astronomy, The Ohio State University, 4055 McPherson Laboratory, Columbus, OH 43210, USA*
[4]*Department of Physics, University of Warwick, Gibbet Hill Road, Coventry CV4 7AL, United Kingdom*
[5]*Observatoire Astronomique de l'Université de Genève, 51 Chemin des Maillettes, CH-1290 Sauverny, Switzerland*
[6]*SUPA, School of Physics & Astronomy, University of St Andrews, North Haugh, St Andrews, Fife, Scotland KY16 9SS, UK*
[7]*Astrophysics Group, Keele University, Staffordshire ST5 5BG, UK*
[8]*NASA Goddard Space Flight Center, 8800 Greenbelt Road, Greenbelt, MD 20771, USA*
[9]*SETI Institute, 189 Bernardo Avenue, Suite 200, Mountain View, CA 94043, USA*
[10]*Department of Astronomy, San Diego State University, 5500 Campanile Drive, San Diego, CA 92182, USA*
[11]*Cavendish Laboratory, J J Thomson Avenue, Cambridge CB3 0HE, UK*

ABSTRACT

A dozen short-period detached binaries are known to host transiting circumbinary planets. In all circumbinary systems so far, the planetary and binary orbits are aligned within a couple of degrees. However, the obliquity of the primary star, which is an important tracer of their formation, evolution, and tidal history, has only been measured in one circumbinary system until now. EBLM J0608-59/TOI-1338 is a low-mass eclipsing binary system with a recently discovered circumbinary planet identified by *TESS*. Here, we perform high-resolution spectroscopy during primary eclipse to measure the projected stellar obliquity of the primary component. The obliquity is low, and thus the primary star is aligned with the binary and planetary orbits with a projected spin–orbit angle $\beta = 2\overset{\circ}{.}8 \pm 17\overset{\circ}{.}1$. The rotation period of 18.1 ± 1.6 d implied by our measurement of $v\sin i_\star$ suggests that the primary has not yet pseudo-synchronized with the binary orbit, but is consistent with gyrochronology and weak tidal interaction with the binary companion. Our result, combined with the known coplanarity of the binary and planet orbits, is suggestive of formation from a single disc. Finally, we considered whether the spectrum of the faint secondary star could affect our measurements. We show through simulations that the effect is negligible for our system, but can lead to strong biases in $v\sin i_\star$ and β for higher flux ratios. We encourage future studies in eclipse spectroscopy test the assumption of a dark secondary for flux ratios $\gtrsim 1$ ppt.

Key words: planets and satellites: formation – binaries: eclipsing – stars: individual: (EBLM J0608-59, TOI-1338) – stars: low-mass – stars: rotation.

1 INTRODUCTION

EBLM J0608-59 consists of an inner low-mass binary ($M_1 = 1.13\,M_\odot$, $M_2 = 0.31\,M_\odot$) on a 14.6-d eccentric orbit (Triaud et al. 2017), with an outer Saturn-sized circumbinary planet on a 95-d orbit recently discovered in *TESS* photometry (TOI-1338 AB b; Kostov et al. 2020). The inner binary was first identified as a transiting planet candidate by the WASP survey (Pollacco et al. 2006), but radial velocities measurements soon determined it was instead a G+M single-lined eclipsing binary. Subsequently, EBLM J0608-59

(hereafter J0608-59) was followed up spectroscopically as part of the EBLM project whose goal is to study the properties of low-mass eclipsing binary systems (Triaud et al. 2013, 2017). One of the objectives of the EBLM project is to provide observational constraints on the tidal physics of tight binaries. To study this, we collect three types of observables: rotational velocities $v_{eq}\sin i_{\star,1}$ of the primary stars, precise eccentricities and, in some cases, spin–orbit angles β,[1] which are obtained by measuring the Rossiter–McLaughlin effect (McLaughlin 1924; Rossiter 1924; Kopal 1942).

---

* E-mail: vxh710@bham.ac.uk (VKH); a.triaud@bham.ac.uk (AHMJT)
† Fulbright Fellow.
‡ Fellow of the Swiss National Science Foundation.

[1]the notation λ has been used for the spin–orbit angle of exoplanets, with $\lambda = -\beta$. β, defined by Kopal (1942), i.e. the projected angle between the orbital and stellar spin axes, is widely used within the binary star community.

Despite many spin–orbit measurements obtained on transiting exoplanets (e.g. Winn & Fabrycky 2015; Triaud 2018), not many have been obtained on eclipsing binaries. A list of historical measurements can be found in Albrecht et al. (2011). Hale (1994) notes that binaries with separation >30–40 au are usually found with random spins. For tighter binaries, the most extensive collection of measurements were produced by the BANANA survey (e.g. Albrecht et al. 2014), which mainly targets massive stars, with a recent compilation from the Torun project (Sybilski et al. 2018). So far, most binary pairs appear spin–orbit aligned except DI Hercules (Albrecht et al. 2009), CV Velorum (Albrecht et al. 2014), and AI Phe (Sybilski et al. 2018). The binary sample covered by the EBLM project is distinct from these other efforts in focusing exclusively on small ($M_2/M_1 \lesssim 0.3$) mass ratio binaries with solar-like primaries. So far, three measurements of β have been published by the project: WASP-30, EBLM J1219-39 (Triaud et al. 2013), and EBLM J0218-31 (Gill et al. 2019), where all primary stars were found to be coplanar with their respective orbits. We have collected Rossiter–McLaughlin measurements on dozens of systems whose analysis are ongoing, exploring parameter space in terms of $v_{eq}\sin i_{\star,1}$, eccentricities, and orbital periods.

In this paper, we report a spectroscopic primary eclipse of J0608-59 to measure the stellar obliquity of the primary component with respect to the binary and planet orbits from the Rossiter–McLaughlin effect. J0608-59 is only the second primary star host to a circumbinary planet to have a Rossiter–McLaughlin measurement made, following the 41 d binary Kepler-16, which was found to be aligned (Winn et al. 2011). Additionally, the 7.5 d binary Kepler-47 is also thought to be spin–orbit aligned, based on eclipse spot-crossings (Orosz et al. 2012).

2 OBSERVATIONS

A single spectroscopic primary eclipse of J0608-59 was observed on 2010 November 2 using the 1.2-m Swiss *Euler* Telescope at La Silla, Chile. The CORALIE instrument spans the visible range (390–680 nm) with an average resolving power of $R \sim 55\,000$. We obtained 19 exposures of 900 s each[2] over 5.8 h, capturing the primary eclipse entirely, including two spectra before ingress. The data were reduced using the standard CORALIE Data Reduction Software (DRS; Lovis & Pepe 2007). In brief, a cross-correlation function (CCF) is derived between the observed spectra and a G2 numerical mask. A comparison is made with a reference thorium–argon spectrum, which allows for corrections based on instrumental variations throughout the eclipse (e.g. atmospheric variations since CORALIE is not pressure stabilized). Overall, CORALIE is stable to 5 m s^{-1}, while the median radial velocity error per observation is 26 m s^{-1}.

As a part of the EBLM program, J0608-59 received an additional 19 radial velocity measurements to map out its orbit with CORALIE. From these data, we select three epochs between 2009 November 28–29 and 2010 January 6 as reference spectra due to insufficient data outside the spectroscopic eclipse night. J0608-59 was also selected as a target in the BEBOP radial velocity search for circumbinary planets. An additional 17 CORALIE measurements were made and published in Martin et al. (2019), and an additional seven HARPS measurements have been taken since. Finally, J0608-59 was observed in 12 *TESS* sectors (Kostov et al. 2020), 9 of which were short-cadence data under the Guest Investigator Program

[2]Except the two initial points, which were 600 s.

Table 1. Target and binary orbital parameters. Subscripts 1 and 2 denote the primary and secondary components, respectively. Brackets denote uncertainties on last two digits.

Parameter	Description	Value
Target information		
α	Right ascension	$06^h08^h31\overset{s}{.}95$
δ	Declination	$-59°32'28''.1$
V_{mag}	Apparent magnitude	11.73
Stellar parameters		
M_1 (M$_\odot$)	Primary mass	1.127(68)
M_2 (M$_\odot$)	Secondary mass	0.313(11)
R_1 (R$_\odot$)	Primary radius	1.331(24)
R_2 (R$_\odot$)	Secondary radius	0.3089(56)
$T_{eff,1}$ (K)	Primary temperature	6050(80)
$T_{eff,2}$ (K)	Secondary temperature	3330(50)
$\log g_1$ (cgs)	Surface gravity	4.00(08)
[Fe/H]$_1$	Metallicity	0.01(05)
$^a v_{eq}\sin i_{\star,1}$ (km s^{-1})	Projected rotation	3.6(0.6)
Age (Gyr)	Isochrone binary age	4.4(0.2)
Orbital parameters		
P_{bin} (d)	Binary orbital period	14.608559(13)
T_{pri} (BJD$-x^b$)	Time of primary eclipse	53336.8242(25)
K_1 (km s^{-1})	RV semi-amplitude	21.6247(34)
e_{bin}	Eccentricity	0.15603(15)
ω_{bin} (°)	Periastron angle	117.554(72)
i_{bin} (°)	Orbital inclination	89.70(18)
b_{bin} (R$_1$)	Impact parameter	0.097(57)
a_{bin} (au)	Separation	0.1321(24)
J_{TESS}	Surface brightness ratio	0.0926(28)
u	Lin. limb darkening coeff.	0.40
v	Quad. limb darkening coeff.	0.29

^{a}Determined from rotational line broadening using HARPS (Kostov et al. 2020).
$^b x = 2\,450\,000$.

G011278 (PI: O. Turner). The BEBOP data were not used in the analysis of this work, but we use orbital parameters (Table 1) from Kostov et al. (2020) that are based on the BEBOP and *TESS* data.

3 LINE PROFILE ANALYSIS

Radial velocity measurements are typically determined from a cross-correlation technique. The resulting CCFs are fitted with Gaussian profiles to determine the effective radial velocity, i.e. treating any distortion of the line profiles as a pure Doppler shift of the line centre. The Rossiter–McLaughlin effect is, however, a spectroscopic effect where the line profiles are distorted depending on the position of the occulting body on the stellar disc.

While many techniques have been put forth to improve on the modelling of the anomalous radial velocity during a spectroscopic transit/eclipse to account for these effects (e.g. Albrecht et al. 2007; Hirano et al. 2011), other methods have been developed for modelling the spectral line distortions directly. These methods are commonly referred to as Doppler tomography or Doppler shadow (Collier Cameron et al. 2010; Cegla et al. 2016a; Hirano et al. 2020). Here, we use the *reloaded* Rossiter–McLaughlin technique from Cegla et al. (2016a) to directly retrieve the occulted light from the stellar disc with no assumptions on the shape of the line profiles compared to other methods. For this and future analyses, we have written a dedicated

software package, `elle`,[3] and plan to release a user-friendly public version in a forthcoming paper.

3.1 Retrieving the occulted light

We work on the disc-integrated CCFs output from the CORALIE DRS. We start by removing the Keplerian velocity due to the binary orbit by resampling the CCFs on a common velocity grid at the spectrograph resolution of $\sim$1.8 km s^{-1}. The orbital parameters to compute the Keplerian model are obtained from Kostov et al. (2020), who analysed the full *TESS* Cycle 1 photometry and CORALIE/HARPS radial velocities, modelling both the binary orbit as well as the circumbinary planet orbit using a photodynamical model. Their fit did not detect any significant binary apsidal motion, and produced a $\chi_\nu^2 \approx 1$, indicating very good agreement on the data despite that $\sim$10 yr separating the first CORALIE observations from the *TESS* photometry. From this, we can rule out any significant changes in the binary ephemeris, such as radial velocity drifts and associated light traveltime effects due to distant massive companions.

The CCFs are scaled by their respective continuum flux to compare their relative flux variations. We define the continuum level as the median flux 4σ outside the computed line profile centres (radial velocity), where σ denotes the width of the Gaussian fit from the CORALIE DRS. In the same fashion, we also estimate the CCF error by computing the standard deviation of the continuum flux. Furthermore, we also normalize the CCFs by the theoretical primary eclipse limb-darkened light curve to account for the loss of light during eclipse, where the light curve was again computed using orbital elements from Kostov et al. (2020).

As with any Doppler shadow method, the in-eclipse CCFs need to be compared to a high SNR template CCF (typically an average over several out-of-eclipse spectra) that represents the intrinsic rotationally broadened stellar spectrum. The Rossiter–McLaughlin sequence we use in this work only has two spectra taken outside of the eclipse window, both observed at high airmass, $z > 1.8$, and at shorter integration times than in-eclipse observations. Upon inspection of the normalized CCFs we noticed – other than lower SNR – that these two observations had CCF contrasts (depths) 3–4 per cent smaller than the remaining sample from the same night.

To avoid biasing our measurements due to the anomalous CCF contrast, we do not use the two spectra at the beginning of night to build our reference. Instead, we average the two spectra together to determine the systemic velocity at the night of the spectroscopic eclipse, γ_{RM}. Then, we identify three individual spectra taken at different nights with the same exposure time as our in-eclipse observations, and verify that their CCF contrast, FWHM, and SNR match the data taken during eclipse. The three reference spectra are resampled to the same grid as with the in-eclipse spectra, but shifted to γ_{RM} to account for any stellar activity between the observations. The three spectra are then averaged together, weighted by their errors, to create a master out-of-eclipse template, CCF$_{out}$. The in-eclipse spectra and CCF$_{out}$ – now in the same reference frame – are then shifted by γ_{RM} to bring the CCFs to the stellar rest frame. The residual line profiles are then calculated from the difference between CCF$_{out}$ and the in-eclipse, disc-integrated CCFs. The resulting in-eclipse residual profiles,[4] hereafter CCF$_{in}$, represent the light on the stellar disc occulted by the star and are shown in Fig. 1, clearly
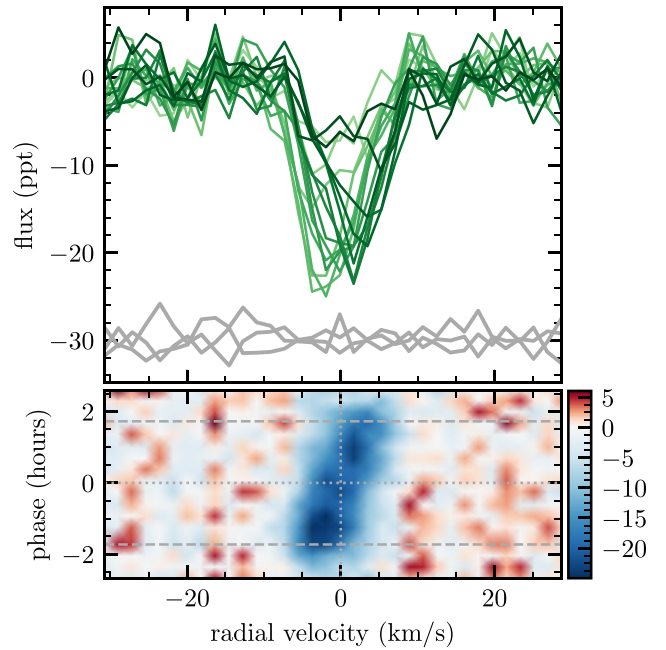

Figure 1. *Upper panel:* The retrieved residual line profiles hidden beneath the eclipsing secondary star, with colours getting darker with time. The grey profiles at the bottom are the residuals from the reference spectra with an arbitrary offset. *Lower panel:* Another view showing the residual flux as a function of time on the vertical axis, displaying the trace, or Doppler shadow, of the eclipsing body moving across the rotating stellar disc. The grey-dashed lines denote the second and third contact points, and the dotted lines denote the mid-transit point and minimum limb angle. The colour bar shows the CCF flux.

displaying the trace of the secondary star as it moves across the primary's disc.

We compute their local radial velocity by fitting Gaussian profiles to the CCF$_{in}$. To obtain realistic uncertainties and avoid fitting spurious signals (particularly an issue for low-SNR data, such as profiles at the stellar limb) we use a Markov chain Monte Carlo (MCMC) sampling method to explore the full posterior distribution and propagate uncertainties in the 'nuisance'[5] parameters to the final radial velocity. We build our Gaussian model in the `pyMC3` framework (Salvatier, Wiecki & Fonnesbeck 2016), varying the line centre, μ; width, σ; contrast A; continuum level, c, and CCF error, ϵ. We sample these five parameters using the No-U-Turn sampler (Hoffman & Gelman 2014). To avoid cherry-picking the local profiles that provide a good fit (and thus keep for further analysis), we use wide, informative priors on our parameters aimed at returning a conservative estimate of the radial velocity in case of a non-detection of the local line centre. The priors for A, σ, and ϵ are drawn from the half-normal distribution as they are both restricted to positive values, and draw from the normal distribution for μ and c. The resulting local surface velocities over the eclipse duration are shown in Fig. 2.

3.2 Surface velocity modelling

The surface velocity model is computed using the semi-analytical prescription in Cegla et al. (2016a). Here, we create a 51 × 51 grid

---

[3]https://github.com/vedad/elle
[4]These are no longer disc-integrated profiles since the disc-integrated contribution has been removed.

[5]While the depths and widths of the Gaussian can be useful for diagnostic purposes, we are mainly interested in the line profile centre, μ, and its uncertainty.
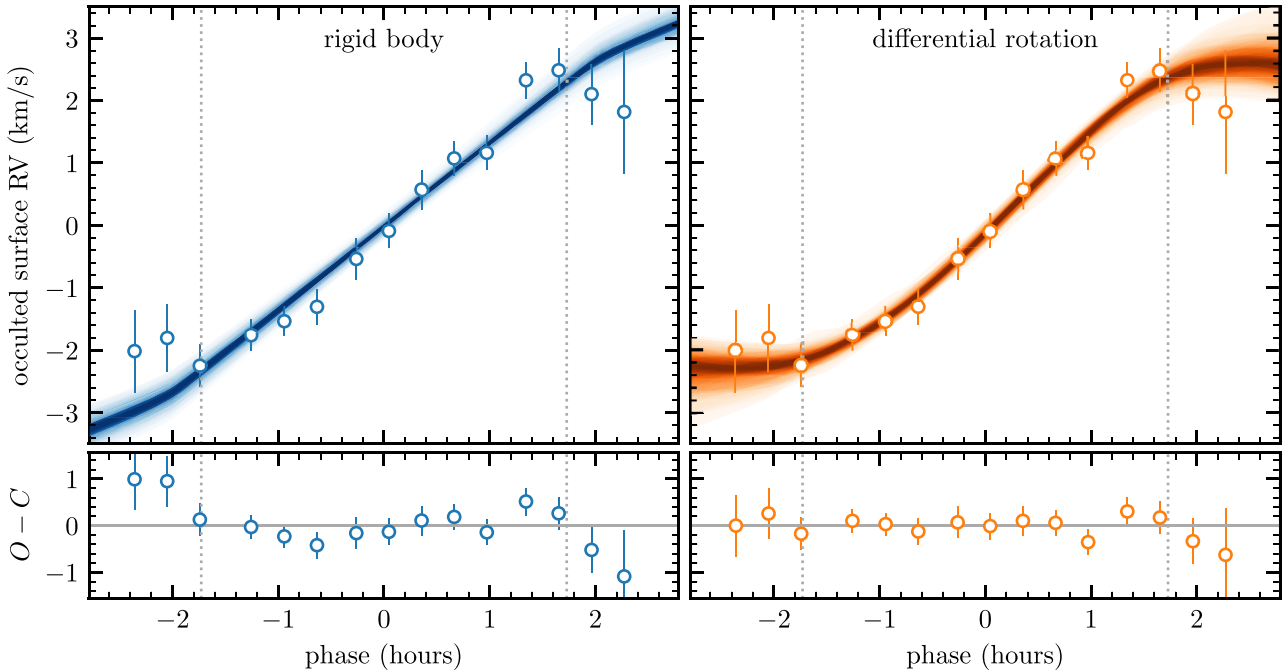
Figure 2. *Upper panels:* The local radial velocities during eclipse, obtained from Gaussian fits to the residual profiles in Fig. 1, for the rigid body model (*left*) and differential rotation model (*right*). The shading denotes the 50th–99th percentiles of the models. The dotted lines denote the second and third contacts, while the horizontal axis is delineated by the eclipse duration. *Lower panels:* Residuals from the maximum likelihood fits of each model. The differential rotation model reduces χ^2_ν from 1.2 to 0.5, and improves the Bayesian Information Criterion (BIC) by 5.5.

that spans the size of the eclipsing body, and co-moving with its centre. At every epoch, the brightness-weighted rotational velocity at a given position is computed by summing the cells covering the stellar disc occulted by the eclipsing body. We assume the star follows a quadratic limb darkening function, with coefficients $c_1 = 0.40$, $c_2 = 0.29$ obtained from interpolating $T_{\rm eff}$, $\log g$, and [Fe/H] in the *V*-band tables from Claret & Bloemen (2011), using the online tool from (Eastman, Gaudi & Agol 2013).[6] Oversampling and averaging our model within each 900 s exposure did not impact our results.

The theoretical surface velocity at any point on a rotating rigid body is computed from a combination of the orbital phase, $\phi(P, T_0)$; orbital inclination, $i_{\rm orb}$; the stellar (primary) radius scaled by the binary separation, R_1/a; projected stellar equatorial velocity, $v_{\rm eq}\sin i_{\star,1}$; and the projected spin–orbit angle, β. While many of these parameters are known very precisely from Kostov et al. (2020; see Table 1), the impact parameter $b = a\cos i_{\rm bin}/R_1$ is known to correlate with both $v_{\rm eq}\sin i_{\star,1}$ and β when b is close to zero. We therefore vary R_1/a and $i_{\rm orb}$ with their Gaussian uncertainties during the fit, and let $v_{\rm eq}\sin i_{\star,1}$ and β float freely. We fix the ephemerides P, T_0, but checked that our results were insensitive to their influence by perturbing them by their 1σ uncertainties. We sample these four parameters using the emcee MCMC sampler (Foreman-Mackey et al. 2013) to obtain their full posterior distributions, using 200 walkers that are run for ∼50 times the autocorrelation length. The final posterior distributions are obtained after discarding a number of burn-in steps determined visually, and thinning the individual walkers by the autocorrelation length of the parameters. We also attempt to model the data assuming the rotation rate varies as a function of stellar latitude (differential rotation). In this case, we

can independently sample the equatorial velocity, $v_{\rm eq}$, and the stellar inclination, $i_{\star,1}$. Additionally, we sample the relative shear, $\alpha = (\Omega_{\rm eq} - \Omega_{\rm pole})/\Omega_{\rm eq}$, which describes the relative rotation rate between the poles and the equator.[7] We varied the parameters uniformly in $v_{\rm eq} \in [0, 5.3]\,{\rm km\,s^{-1}}$, $\beta \in [-180, 180]^\circ$, $i_{\star,1} \in [0, 180]^\circ$, and $\alpha \in [-2, 1]$, where $\alpha < 0$ signifies antisolar differential rotation, i.e. that the polar latitudes rotate faster than the equator. The upper limit on $v_{\rm eq}$ was set to the predicted pseudo-synchronous rotation period, which is expected at 12.7 d.

4 RESULTS AND DISCUSSION

4.1 Stellar obliquity and rotation

The trace of the secondary star in Fig. 1 is clearly indicative of a prograde orbit as it moves from blue-shifted to red-shifted areas on the stellar disc of the primary. We summarize our results in Table 2. From the data modelling outlined in Section 3, we find a projected rotation and projected stellar obliquity, $\beta = 2°.8 \pm 17°.1$ when assuming rigid body rotation. The three largest sources of angular momentum in the system are the binary and planetary orbits, followed by the primary's rotation – whose magnitudes contribute in approximate ratios of 6000:4:1. Given that the binary and planet orbits are co-planar, with mutual a inclination $|\Delta i| = 0.3°$, the largest angular momentum vectors are thus found to be aligned. Kostov et al. (2020) reported $v_{\rm eq}\sin i_{\star,1} = 3.6 + -0.6\,{\rm km\,s^{-1}}$ from rotational broadening, based on high-resolution spectra from HARPS obtained through the BEBOP survey (ESO prog. ID 1101.C-0721, PI: Triaud; Martin et al. 2019), thus the two measurements agree very well. Our measurement of $v_{\rm eq}\sin i_{\star,1}$ combined with the stellar radius

---

[6] http://astroutils.astronomy.ohio-state.edu/exofast/limbdark.shtml

[7] $\alpha \sim 0.2$ for the Sun.

Table 2. Derived spin–orbit parameters. The bold values denote adopted values and model.

Model	v_{eq} (km s^{-1})	$i_{\star,1}$ (°)	β (°)	α	ψ (°)	P_{rot} (d)	χ^2	BIC
Rigid body	$\mathbf{3.69^{+0.35}_{-0.25}}$	$\mathbf{90}^a$	$\mathbf{2.9^{+16.0}_{-15.8}}$	$\mathbf{0}^a$	$-$	$\mathbf{18.3^{+1.4}_{-1.6}}$	**15.9**	$\mathbf{-9.2}$
Differential rotation	$3.89^{+0.87}_{-0.68}$	$137.1^{+13.7}_{-74.8}$	$9.7^{+12.4}_{-11.8}$	$[-1.85,\ -0.91]^b$	$53.0^{+10.5}_{-16.4}$	$17.3^{+3.7}_{-3.2}$	4.9	-14.8

^{a}Fixed under rigid body assumption. ^{b}68 per cent confidence interval.

suggests a present-day rotation period of 18.1 ± 1.6 d, assuming a stellar inclination of 90°.

The rigid body model in the left-hand panel of Fig. 2 does not accurately predict the surface velocity at the limbs. One could rightly expect the behaviour at the limb to depend on the particular choice of limb darkening models and its parameters, as well as the size of planet grid. We addressed each of these scenarios by varying the limb darkening coefficients within Gaussian uncertainties of 0.1, using a power-2 limb darkening law (e.g. Maxted 2018), and increasing the planet grid size up to 91×91. None made any detectable impact on our results. Moreover, the centre-to-limb variation due to convective blueshift (Cegla et al. 2016a,b) is expected to be symmetric around the mid-transit time, while the data at both limbs seem to be antisymmetric (dragged towards zero velocity), and thus cannot explain the effect. Most likely the effect is due to correlated noise of an unknown origin, possibly originating from nightly differences between the reference and eclipse spectra. Nevertheless, we verified that our results stayed consistent when only fitting the data between the second and third eclipse contact points, obtaining differences within the 1σ uncertainties of the parameters.

4.2 Formation scenario

Tidal evolution has three relevant effects on a binary: *(i)* alignment of stellar spin axes, *(ii)* synchronization of stellar rotation rates, and *(iii)* circularization of the orbit. The first two effects are believed to occur on a roughly similar time-scale, whereas the circularization is a much slower process, owing to there being significantly more angular momentum in the orbit than in the stars (Hut 1981). J0608-59 is too widely separated ($R_1/a_{bin} = 0.023$) for circularization to have occurred within our estimated lifetime of $\sim$4 Gyr,[8] and so its eccentricity of $e_{bin} = 0.156$ is not surprising.

For non-circular binaries, such as J0608-59, tides do not synchronize the rotation rates with the orbital period (14.61 d). Instead, the stellar rotation will over time pseudo-synchronize with the orbital motion at periastron (Hut 1981). Using their equation (42), the pseudo-synchronous rotation period is 12.7 d for J0608-59. This is significantly shorter than our derived rotation period of 18.1 ± 1.6 d. On the other hand, using the gyrochronological age–rotation relation for single stars from Mamajek & Hillenbrand (2008), the predicted rotation period from stellar spin-down is estimated to be 19.6 ± 2.4 d for our $\sim$4 Gyr star, which may provide a plausible explanation for the measured rotation rate given the binary separation. We therefore suggest that the primary star's rotation rate is largely unaffected by tides from the binary companion, but rather driven by magnetic braking. This result is consistent with fig. 10 of Torres, Andersen & Giménez (2010), showing that binaries with $R_1/a \lesssim 0.1$ are not necessarily pseudo-synchronized, and also remain eccentric.

The fact that the star is not pseudo-synchronized may appear at odds with an aligned projected obliquity of $\sim$0°. However, we

present two simple explanations for this apparent discrepancy. First, the stellar obliquity may too be unaffected by tides, but rather the binary was primordially aligned and such alignment persisted through its evolution. This points to the two stars having formed from gravitational fragmentation within a single disc. If they are formed at an initially wider separation (predicted by e.g. Bate, Bonnell & Bromm 2002), then their orbital shrinkage would be due to accretion and disc migration, and not a more violent scattering event, such that the stellar alignment and circumbinary planet are preserved (Martin 2019). An alternate explanation is that the time-scale of spin alignment, at least in the case of J0608-59, is noticeably shorter than that of pseudo-synchronization.

The Kepler-16 circumbinary planet system, by comparison, has a wider binary ($R_1/a_{bin} = 0.013$) that is also eccentric and spin–orbit aligned, but contrarily has a rotation period equal to that expected from pseudo-synchronization ($\sim$35 d). However, Winn et al. (2011) point out that this rotation rate also agrees well with the expectation from gyrochronology. Our result may support the view that the rotation of Kepler-16 A is only coincidental with the pseudo-synchronous rotation period and has not been synchronized by tides, but has rather spun down to its present rate due to the natural spin-down of stars from magnetic braking. The Kepler-47 circumbinary system is comparatively much tighter ($R_1/a_{bin} = 0.053$) than both J0608-59 and Kepler-16. Tides are most likely responsible for its small eccentricity (0.023), near synchronization ($P_{bin} = 7.448$ d and $P_{rot} = 7.775$ d), and spin–orbit alignment ($<$20°).

4.3 Differential rotation and true obliquity

Although unlikely, it is worth mentioning that the true stellar obliquity may be non-zero, i.e. that the star is pointing either towards or away from us and is thus still realigning. Ordinarily, an independent measurement of the rotation period from spot modulation, together with a projected equatorial rotational velocity from the Rossiter–McLaughlin analysis, can provide a measurement of the stellar inclination. However, Kostov et al. (2020) show that neither *TESS* nor ASAS-SN photometry display any clear periodicity. We show our fit to the differential rotation model in the right-hand panel of Fig. 2. The fit favours a higher stellar inclination, $i_{\star,1} = 137.1^{+13.7}_{-74.8}$ °, with true obliquity $\psi = 50°.4 \pm 13°.4$ and latitudes rotating antisolar with $\alpha < 0$ at the 99th percentile. The implied rotation period here is $17.3^{+3.7}_{-3.2}$ d, which is similar to the rigid body case. The fit improves the Bayesian Information Criterion by 5.5, showing an improvement in the model, although the reduced $\chi^2_\nu = 0.45$ suggests we may be overfitting the data. There have only been detections of antisolar differential rotation in three giant stars (Strassmeier, Kratzwald & Weber 2003; Kővári et al. 2013; Kriskovics et al. 2014), with only a small handful of main-sequence Sun-like candidates (Benomar et al. 2018). Ultimately, we are not able to rule out contributions from correlated noise and therefore consider it unlikely that the star is inclined. We conclude that the rigid body model is the most likely scenario and thus the true obliquity of the star is low.

[8]Derived in Kostov et al. (2020) using stellar isochrones.

4.4 Spectral contamination from secondary star

The systems that make up the EBLM sample (including J0608-59) are single-lined binaries, where the spectrum from the secondary star is too faint to be detected in individual observations. However, if the flux emission from the secondary star exceeds that of the noise in the data, the faint signal of the secondary spectrum may be imprinted in the spectrum that is dominated by the light from the primary star, and impact the shape of the final CCF. Since the reloaded Rossiter–McLaughlin method depends on detecting changes in the CCF shape during eclipse, this may impact our measurements. It is worth noting that for the vast majority of the binary orbit this is still not a problem, as the relative radial velocity motion between the two stars is so large that the line core from the secondary star falls outside the line core of the primary star and will not affect the CCF shape. Most of the contamination will occur close to conjunctions, where their radial velocity curves cross.

The apparent magnitude of the system in the CORALIE *V* band is $m_{V,1} = 11.73$. Assuming an age of 5 Gyr, Triaud et al. (2017) predict an apparent brightness for the secondary star $m_{V,2} = 19.75$, which gives an estimated secondary-to-primary flux ratio of ~ 1 ppt through the relation

$$\Delta m_V = -2.5 \log \left(\frac{F_{V,2}}{F_{V,1}} \right).$$

The fitted noise of the residual CCFs in Fig. 1 is ~ 2.5 ppt, which yields an SNR < 0.5 for the spectrum from the secondary star. The impact of the secondary spectrum should therefore not affect our measurements of $v_{eq}\sin i_{\star,1}$ and β. Despite this, we carry out a simulation to quantify the impact of the secondary spectrum, and how it changes with increasing flux ratio. We simulate a series of CCFs for the primary star during eclipse, centred at the radial velocity of the primary star in the barycentric reference frame, assuming Gaussian profiles with depths and widths determined by their typical observed values. We add uncertainties to the CCFs according to the typically fitted error, ϵ from the MCMC analysis in Section 3.1. We add a CCF from the secondary star, where we assume that the contrast and full width at half-maximum (FWHM) is the same as for the primary, with flux ratio δF, and centred at the predicted radial velocity of the secondary star from the Keplerian orbit, again in the barycentric reference frame. Finally, we assume Gaussian profiles for the distortion due to the Rossiter–McLaughlin effect, with contrasts and FWHM as fitted in Section 3.1, and their radial velocity centres translated to the barycentric reference frame. This contribution is subtracted from our combined CCF from the two stars to simulate the missing light from the occulted disc.

We apply the reloaded Rossiter–McLaughlin effect outlined in Section 3 to our simulated CCFs, which, as described above, include contributions from both stars and the distortion of the line profiles due to an occulted disc. We vary the flux ratio of the secondary using $F_2/F_1 = \{1, 5, 10\}$ ppt, and repeat the MCMC sampling procedure from before to obtain posterior distributions for $v_{eq}\sin i_{\star,1}$ and β. The posterior distributions are shown in Fig. 3. The simulation with $F_2/F_1 = 1$ ppt matches the observed data remarkably well, and does not show any significant bias in the derived parameters when compared to the simulation with a dark secondary. However, the posterior distributions for both parameters become significantly biased for higher flux ratios. Our simulations show that care must be taken for eclipse spectroscopy with luminous secondaries, and potentially even for eclipse spectroscopy of exoplanets due to the hot day-side temperatures of some ultrahot Jupiters, which can reach similar temperatures to M or even K dwarfs. Assuming a flux ratio
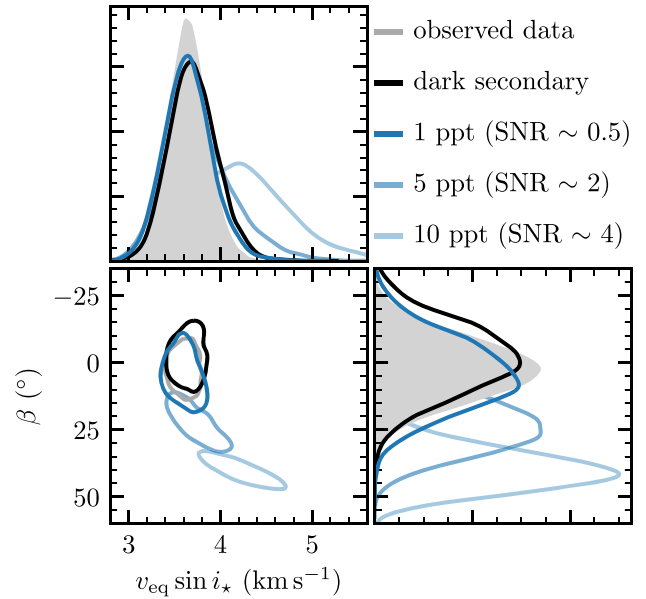

Figure 3. Simulation of the impact of varying levels of emission flux from the secondary star on the retrieved values for $v_{eq}\sin i_{\star,1}$ and β. The posterior distribution for the observed data is shown in grey, and is compared to the simulation with no contamination from a secondary spectrum in black. The coloured lines show the simulated effect for increasing relative flux contribution from the occulting body. The estimated flux contamination for J0608-59 is ~ 1 ppt, which agrees very well with the simulated data. The lower left-hand panel shows the 1σ contours.

of ~ 15 ppt, as for the Kepler-16 system (Doyle et al. 2011), the secondary spectrum could bias the measurement of β to $> 30°$ at 3σ significance, and overestimate $v_{eq}\sin i_{\star,1}$ by $\simeq 30$ per cent.

A few caveats are worth mentioning with the simulations. First, the relative depth and width of the secondary CCF are assumed to be the same as for the primary CCF. This may not always be the case when the spectral types of the stars are very different. Taking a G-M binary as an example, the convolution of an M dwarf spectrum with a G2 mask can yield shallower (thus lower SNR) CCFs than assumed here due the cross-correlation with template lines that are not present in M dwarf spectra. In practice, the simulations we carry out here present a worst-case scenario. Secondly, the impact of the secondary spectrum will also depend on the specific orbital characteristics, in particular the eccentricity and argument of periastron, which determine where and how much the two spectra will overlap.

5 CONCLUSIONS

We have presented a stellar obliquity measurement of the primary star in the EBLM J0608-59/TOI-1338 eclipsing binary system, recently discovered to host a circumbinary planet. High-resolution spectroscopy during primary eclipse supports a low obliquity, consistent with alignment with the binary and planet orbits. The binary orbit has not pseudo-synchronized, which indicates that the obliquity of the star has not been influenced by tides, and is thus likely primordial. Moreover, we have simulated the effect of an unresolved secondary spectrum on our analysis of eclipse spectra, and show that the effect is negligible for our data. However, secondaries that contribute with flux of just a few thousandths of that of their primaries can strongly bias measurements of $v_{eq}\sin i_{\star,1}$ and β.

J0608-59 is but one of ~ 20 EBLM systems for which we are currently studying stellar obliquities from Rossiter–McLaughlin

sequences observed with CORALIE and HARPS, and currently the only one known to host a circumbinary planet. However, our sample has significant overlap with the BEBOP Doppler survey for circumbinary planets therefore we may soon find more similar systems. In a forthcoming paper, we will present obliquity measurements on ∼20 systems observed with CORALIE and HARPS, which will allow us to place constraints on tidal evolution in low-mass binaries and their circumbinary planets.

DATA AVAILABILITY

The data underlying this article will be shared on reasonable request to the corresponding author.

REFERENCES

Albrecht S., Reffert S., Snellen I., Quirrenbach A., Mitchell D. S., 2007, A&A, 474, 565
Albrecht S., Reffert S., Snellen I. A. G., Winn J. N., 2009, Nature, 461, 373
Albrecht S. et al., 2011, ApJ, 738, 50
Albrecht S. et al., 2014, ApJ, 785, 83
Bate M. R., Bonnell I. A., Bromm V., 2002, MNRAS, 336, 705
Benomar O. et al., 2018, Science, 361, 1231
Cegla H. M., Lovis C., Bourrier V., Beeck B., Watson C. A., Pepe F., 2016a, A&A, 588, A127
Cegla H. M., Oshagh M., Watson C. A., Figueira P., Santos N. C., Shelyag S., 2016b, ApJ, 819, 67
Claret A., Bloemen S., 2011, A&A, 529, A75
Collier Cameron A., Bruce V. A., Miller G. R. M., Triaud A. H. M. J., Queloz D., 2010, MNRAS, 403, 151
Doyle L. R. et al., 2011, Science, 333, 1602
Eastman J., Gaudi B. S., Agol E., 2013, PASP, 125, 83
Foreman-Mackey D., Hogg D. W., Lang D., Goodman J., 2013, PASP, 125, 306
Gill S. et al., 2019, A&A, 626, A119
Hale A., 1994, AJ, 107, 306
Hirano T., Suto Y., Winn J. N., Taruya A., Narita N., Albrecht S., Sato B., 2011, ApJ, 742, 69
Hirano T. et al., 2020, ApJ , 890, L27
Hoffman M. D., Gelman A., 2014, J. Mach. Learn. Res., 15, 1593
Hut P., 1981, A&A, 99, 126
Kopal Z., 1942, ApJ, 96, 399
Kostov V. B. et al., 2020, AJ, 159, 253
Kriskovics L., Kővári Z., Vida K., Granzer T., Oláh K., 2014, A&A, 571, A74
Kővári Z., Korhonen H., Strassmeier K. G., Weber M., Kriskovics L., Savanov I., 2013, A&A, 551, A2
Lovis C., Pepe F., 2007, A&A, 468, 1115
Mamajek E. E., Hillenbrand L. A., 2008, ApJ, 687, 1264
Martin D. V., 2019, MNRAS, 488, 3482
Martin D. V. et al., 2019, A&A, 624, A68
Maxted P. F. L., 2018, A&A, 616, A39
McLaughlin D. B., 1924, ApJ, 60, 22
Orosz J. A. et al., 2012, Science, 337, 1511
Pollacco D. L. et al., 2006, PASP, 118, 1407
Rossiter R. A., 1924, ApJ, 60, 15
Salvatier J., Wiecki T. V., Fonnesbeck C., 2016, Peer J Comput. Sci., 2, e55
Strassmeier K. G., Kratzwald L., Weber M., 2003, A&A, 408, 1103
Sybilski P., Pawłaszek R. K., Sybilska A., Konacki M., Hełminiak K. G., Kozłowski S. K., Ratajczak M., 2018, MNRAS, 478, 1942
Torres G., Andersen J., Giménez A., 2010, A&AR, 18, 67
Triaud A. H. M. J., 2018, Handbook of Exoplanets, Springer, p. 2
Triaud A. H. M. J. et al., 2013, A&A, 549, A18
Triaud A. H. M. J. et al., 2017, A&A, 608, A129
Winn J. N., Fabrycky D. C., 2015, ARA&A, 53, 409
Winn J. N. et al., 2011, ApJ, 741, L1

This paper has been typeset from a TEX/LATEX file prepared by the author.